Atmospheric Research 144 (2014) 57–72

Contents lists available at ScienceDirect

Atmospheric Research

journal homepage: www.elsevier.com/locate/atmos

A monostatic microwave transmission experiment for line integrated precipitation and humidity remote sensing

Christian Chwala [a,*], Harald Kunstmann [a,b], Susanne Hipp [c], Uwe Siart [c]

[a] Karlsruhe Institute of Technology, Institute of Meteorology and Climate Research Garmisch-Partenkirchen, Germany
[b] University of Augsburg, Institute of Geography, Augsburg, Germany
[c] Technische Universität München, Institute for High Frequency Engineering, Munich, Germany

ARTICLE INFO

Article history:
Received 15 April 2012
Received in revised form 8 May 2013
Accepted 21 May 2013
Available online 9 July 2013

Keywords:
Precipitation
Humidity
Remote sensing
Microwave remote sensing
Weather radar

ABSTRACT

Near-surface water vapor and precipitation are central hydrometeorological observables which are still difficult to quantify accurately above the point scale. Both play an important role in modeling and remote sensing of the hydrologic cycle. We present details on the development of a new microwave transmission experiment that is capable of providing line integrated estimates of both humidity and precipitation near the surface. The system is located at a hydrometeorological test site (TERENO-prealpine) in Southern Germany. Path length is kept short at 660 m to minimize the likelihood of different precipitation types and intensities along the path. It uses a monostatic configuration with a combined transmitter/receiver unit and a 70 cm trihedral reflector. The transmitter/receiver unit simultaneously operates at 22.235 GHz and 34.8 GHz with a pulse repetition rate of 25 kHz and alternating horizontal and vertical polarization, which enable the analysis of the impact of the changing drop size distribution on the rain rate retrieval. Due to the coherence and the high phase stability of the system, it allows for a sensitive observation of the propagation phase delay. Thereof, time series of line integrated refractivity can be determined. This proxy is then post-processed to absolute humidity and compared to station observations. We present the design of the system and show an analysis of selected periods for both, precipitation and humidity observations. The theoretically expected dependence of attenuation and differential attenuation on the DSD was reproduced with experimental data. A decreased performance was observed when using a fixed A–R power law. Humidity data derived from the phase delay measurement showed good agreement with in situ measurements.

1. Introduction

The accurate quantification of water vapor and precipitation in time and space is still challenging with the established methods, like rain gauges, climate stations and radar.

Rain rate observations with rain gauges are only point measurement lacking spatial representativeness, in particular during convective events of small spatial size. Additional uncertainties are introduced by wind and exposure-induced errors (Sevruk and Zahlavova, 1994; Nešpor and Sevruk, 1999). In contrast to rain gauges, weather radar observations have a high spatial coverage. However, results of radar observations are impaired by the error-prone relation of measured reflectivity and rain rate (Ulbrich and Lee, 1999), variability of the vertical profile of reflectivity (Smith et al., 1986; Hazenberg et al., 2011), (partial) beam blockage and enhanced bright band interception (Andrieu et al., 1997). The latter are particularly increased in mountainous regions.

Terrestrial microwave point-to-point links, with basic ideas from radar attenuation research performed in the 1960s and 1970s (Atlas, 1964; Atlas and Ulbrich, 1977), are currently becoming a popular new tool to gather additional information

* Corresponding author. Tel.: +49 8821 183246.
E-mail address: christian.chwala@kit.edu (C. Chwala).

http://dx.doi.org/10.1016/j.atmosres.2013.05.014
0169-8095

on precipitation. Attenuation data from purpose-built microwave propagation links has been used for several applications of precipitation remote sensing (Ruf et al., 1996; Rincon and Lang, 2002; Holt et al., 2003; Rahimi et al., 2003; Upton et al., 2005; Minda and Nakamura, 2005; Leijnse et al., 2007b). Only recently, this technique was transferred to the existing network of commercial microwave links comprising the backhaul of the cell phone network (Messer et al., 2006; Leijnse et al., 2007c; Zinevich et al., 2008; Schleiss and Berne, 2010; Overeem et al., 2011; Chwala et al., 2012).

Observation techniques for absolute humidity (also referred to as moisture or water vapor) also experienced improvements. Besides basic operational surface station and radiosonde measurements with limited spatial representativeness, new retrieval techniques were developed. Attenuation data from satellite up- and downlinks operating at 22.235 GHz was used for absolute humidity retrieval (Cuccoli et al., 2001). The same principle was applied to the commercial microwave backhaul link network (David et al., 2009). A different approach is exploiting time delay from the Global Positioning System (GPS). Measurements are performed using both ground-based and satellite-based GPS receivers (Bevis et al., 1992; Ware et al., 1996). High spatial resolutions area are achieved using satellite measurements, e.g. from the Moderate Resolution Imaging Spectroradiometer (MODIS), although associated with reduced temporal resolution. A further new method providing good spatial and temporal near-surface estimates of absolute humidity using radar phase delay measurements was introduced by Fabry et al. (1997) and was tested successfully during the International H2O Project (IHOP) (Weckwerth et al., 2005) and the REFRACTT project (Roberts et al., 2008).

Here we present a system to study retrieval methods for both, precipitation and absolute humidity using microwave attenuation as well as phase delay data. In the following sections we briefly introduce the basic theory behind the retrieval methods. We describe the system details and conclude with the evaluation of measurements made over selected periods.

2. Interaction of microwave radiation with the atmosphere: A brief overview

The propagation of microwave radiation through the atmosphere is affected by many variables like pressure, absolute humidity, temperature, suspended water droplets, oxygen, and precipitation. It has been studied in detail (e.g. Liebe, 1989) to allow for estimations of disturbances in microwave communication or, the other way round in remote sensing, for retrieval of atmospheric parameters from those disturbances. Here we will focus on the extraction of liquid precipitation and humidity information from microwave attenuation and phase delay.

2.1. Microwave radiation and precipitation

2.1.1. Attenuation

As already described in theory by Stratton (1930) and proven by measurements of Mueller (1946), rainfall considerably attenuates radiation in the microwave regime ($\lambda < 10$ cm).

This attenuation $A(R)$ in dB/km for a certain rain rate R in mm/h can be calculated as

$$A(R) = 4.343 \times 10^3 \int_0^\infty C_{\text{ext}}(D) N(D,R) dD \quad (1)$$

where $C_{\text{ext}}(D)$ is the scattering cross section in m^2 of a drop with diameter D in mm. $N(D,R)$ is the drop number concentration per cubic meter and per millimeter diameter interval, also referred to as drop size distribution (DSD), which can be described by

$$N(D,R) = N_0(R) D^\mu e^{-\Lambda(R) D} \quad (2)$$

with $\Lambda = \alpha R^{-\beta}$ in mm^{-1} and N_0 in $\text{mm}^{-(1-\mu)}\ \text{m}^{-3}$ (Ulbrich, 1983). Table 1 gives four different sets of the parameters N_0, μ, and Λ to produce different theoretical drop size distribution. They will be used as comparison in Section 5.1.

For a given $N(D,R)$ the rain rate

$$R = 0.6 \times 10^{-3} \pi \int_0^\infty v(D) D^3 N(D,R) dD \quad (3)$$

can be calculated with the drop fall velocity $v(D)$ in m/s. This velocity can be assumed to be the terminal velocity $v_t(D)$ of the drops falling in still air, which Beard (1976) could describe accurately with a physical model. An approximation of this model is given by Mätzler and Martin (2003) which allows us to calculate terminal velocity at standard air pressure of 1013 hPa as

$$v_t(D) = \begin{cases} 0 & \text{if } D \le 0.03 \text{ mm} \\ 4.323(D - 0.03) & \text{if } 0.03 \text{ mm} < D \le 0.6 \text{ mm} \\ 9.65 - 10.3\, e^{-0.6\, D} & \text{if } D > 0.6 \text{ mm} \end{cases} \quad (4)$$

where $v_t(D)$ is in m/s and the drop diameter D in mm.

From Eqs. (1) and (3) it can be seen that the relation between A and R will depend on the relation of their different integrands $v(D)D^3$ and $C_{\text{ext}}(D)$.

To analyze this dependence and to be able to derive A for a given DSD, calculations of $C_{\text{ext}}(D)$ have been carried out using the T-Matrix method introduced by Waterman (1971), for which the source code (Mishchenko, 2000) is freely available. An oblate spheroid shape, with axis ratios according to Pruppacher and Beard (1970), was used. This drop asymmetry results in different values of $C_{\text{ext}}(D)$ for horizontal and vertical polarization. For the calculation of the refractive index of water, following the equations given by Liebe et al.

Table 1
Parameters of Eq. (2) for the drop size distribution (DSD) of Marshall and Palmer (1948), the two types of Joss and Waldvogel (1969) for drizzle and thunderstorm, and a representation of the Laws and Parsons (1943) DSD taken from (Wolf, 2001). JD and JT are two extreme cases which result in DSDs with a very small and a very large number of large drops, respectively. MP and LP should be representative for common wide spread rain events, where LP makes use of the shape parameter μ which, when positive, decreases the number of small drops.

Type	Abbreviation	N_0 in $\text{mm}^{-(1-\mu)}\ \text{m}^{-3}$	μ	Λ in mm^{-1}
Marshall Palmer	MP	0.80×10^4	0	$4.10R^{-0.210}$
Joss Drizzle	JD	3.00×10^4	0	$5.70R^{-0.210}$
Joss Thunderstorm	JT	0.14×10^4	0	$3.00R^{-0.210}$
Laws-Parson	LP	$1.98 \times 10^4 R^{-0.384}$	2.93	$5.38R^{-0.186}$

(1991), a water temperature of 10 °C was used. Changing the shape model to normalized Chebyshev shapes (Chuang and Beard, 1990) or changing the temperature to 0 °C or 10 °C has only little effect: e.g. a change by 10 °C results in a deviation smaller than 5% for drops larger than 2 mm, which is small compared to the effect variations in N(D) have on the calculation of A.

Fig. 1-a1 and b1 shows the calculated values of $C_{ext}(D)$ for the two frequencies used in the transmission experiment (22.235 GHz and 34.8 GHz). Drop diameters were restricted to $D < 6$ mm, which is regarded as the upper limit for rain drop size here. As already pointed out by Atlas and Ulbrich (1977) and Leijnse et al. (2007b), $v_t D^3$ and C_{ext} have almost the same slope in the log–log plot for 35 GHz, which explains the almost linear relation between A and R at this frequency and which also indicates a low dependency on the DSD. The deviation for drops larger than approximately 2.5 mm can, however, alter this relation if a sufficient number of large drops are present in the rain event. As Aydin and Daisley (2002) explained, the diameter at which this deviation starts depends on the transition from Rayleigh scattering to resonance scattering. This takes place when the size parameter x is

$$x = \frac{\pi D \times 10^{-3}}{\lambda} \approx 1 \tag{5}$$

where λ is the wavelength in m. For 34.8 GHz this is true at $D \approx 2.7$ mm. This can also be seen by looking at the extinction efficiency Q_{ext} (which is C_{ext} normalized by the projected area of the drop) shown in Fig. 1-a3 where the main resonance peak can be found around 2.7 mm.

For 22.235 GHz the deviation from the slope of $v_t D^3$ is more pronounced, which leads to a less linear relation between A and R at this frequency. Due to the longer wavelength, the resonance scattering becomes dominant at a larger diameter than at 34.8 GHz. The asymmetry of the drops is thus larger at

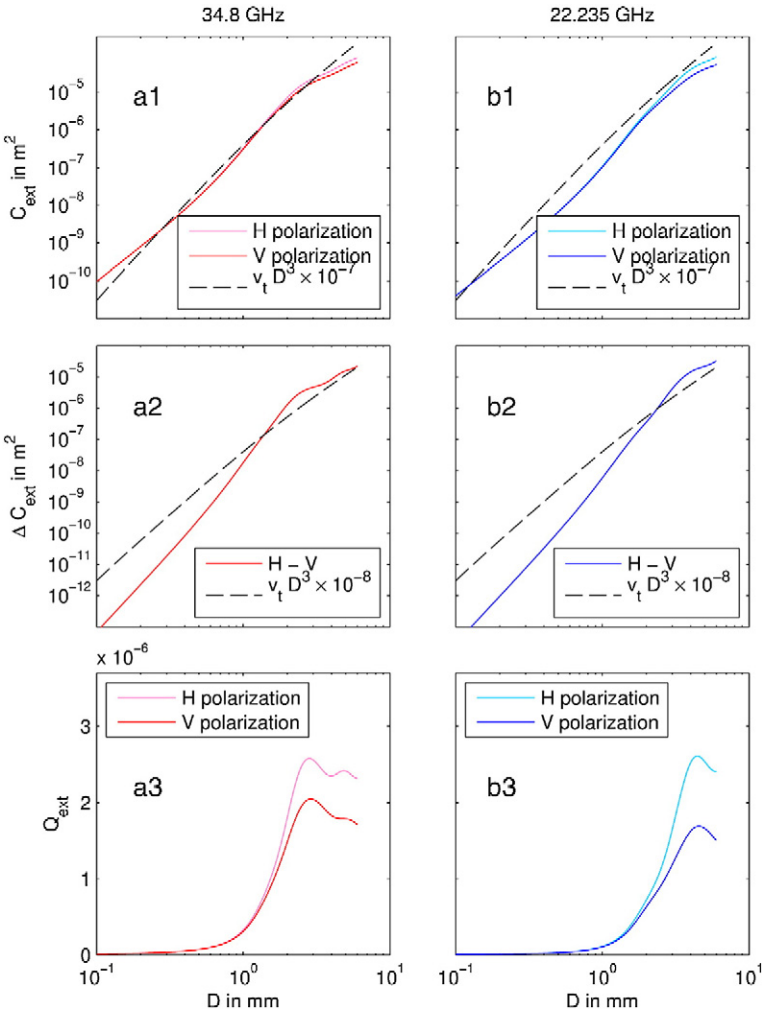

Fig. 1. Extinction cross sections C_{ext}, differential extinction cross sections ΔC_{ext} and extinction efficiency Q_{ext}, for 34.8 GHz and 22.235 GHz for both, horizontal and vertical polarization. Drop shape is assumed to be and oblate spheroid with axis rations according to Pruppacher and Beard (1970). The refractive index of water was calculated according to Liebe et al. (1991) for a water temperature of 10 °C.

the 22.235 GHz resonance peak. Hence the difference between C_{ext} for horizontal and vertical polarization is more pronounced at 22.235 GHz than at 34.8 GHz for drop diameter D > 4 mm. $C_{ext,22,h}$ even exceeds $C_{ext,35,h}$ for large drops (the indices of C_{ext} indicate the frequency and polarization). That is, in the presence of large drops the attenuation and differential attenuation at 22.235 GHz can be very close to the values at 34.8 GHz, or even exceed them.

In general, the differential cross-section $\Delta C_{ext} = C_{ext,H} - C_{ext,V}$, shown in Fig. 1-a2 and b2, exhibits a larger deviation from the slope of $v_t D^3$. That leads to a nonlinear relation between the differential attenuation $\Delta A = A_h - A_v$ and R. ΔA will hence also be more sensitive to changes in the DSD than A. Since ΔC_{ext} is smaller than $C_{ext,H}$, ΔA will also be less sensitive to rain in general (note, that $v_t D^3$ was scaled with $\times 10^{-8}$ here). Thus, it is not optimal for estimating the rain rate when used without additional measurements, e.g. of A. However, its stronger dependence on the DSD can allow the detection of changes in the DSD. Furthermore it should not be sensitive to disturbances like the effect of wet antenna, since it only depends on the axial ratio of the drop diameter.

The values of C_{ext} discussed here and shown in Fig. 1 will be used in Section 5.1 to derive attenuation values from the DSD measured by the disdrometer at the test site.

2.1.2. The A–R power law relation

Since in most cases no in situ data of the DSD is available to derive a relation between A and R, approximations of this relation are needed. According to theoretical and experimental studies (Atlas and Ulbrich, 1977; Olsen et al., 1978), the relation between attenuation A in dB/km and rain rate R in mm/h can be approximated by the power law

$$A = a\, R^b \tag{6}$$

with a and b being constants depending on frequency, temperature and drop size distribution (DSD). Hence for different assumed or measured DSDs, different sets of values of a and b are valid. In Section 5.1 we use the a and b values given by the recommendation of the *International Telecommunication Union* (ITU, 2003). No details are given here which DSD model and temperature was used to derive a and b. Comparison with power law fits to the theoretical DSDs listed in Table 1 (not shown here) suggests that a DSD similar to the MP type has been used. For all values of a and b in between the tabulated ones we perform a shape-preserving spline interpolation as shown in Fig. 2a. Expected attenuation values for frequencies of 34.8 GHz and 22.235 GHz, which are used in the experiment, are shown in Fig. 2b. The corresponding values for a and b are shown in Table 2.

2.1.3. The ΔA–R power law relation

The calculations of the extinction cross section C_{ext} in Section 2.1.1 showed, that ΔC_{ext} and hence $\Delta A = A_h - A_v$ are also sensitive to rain rate, since the shape of falling raindrops considerably deviates from a sphere for larger drops. With $A_{f,h}$ and $A_{f,v}$ being the attenuation values for the different polarizations and the operating frequency f in GHz, we define the differential attenuation

$$\Delta A_{f,} = A_{f,h} - A_{f,v}. \tag{7}$$

Employing the a and b values from Section 2.1.2 a non-linear least square fit of the power law

$$\Delta A_f = a_{\Delta f} R^{b_{\Delta f}} \tag{8}$$

yields $a_{\Delta 22} = 0.01$, $b_{\Delta 22} = 1.24$ and $a_{\Delta 35} = 0.031$, $b_{\Delta 35} = 1.07$. The resulting relation between rain rate and attenuation is shown in Fig. 2c. The values for $f = 35$ GHz are close to the ones found by Atlas and Ulbrich (1977), $a_\Delta = 0.039$ and $b_\Delta = 1$. Ruf et al. (1996) also found a linear relation to fit best with $a_\Delta = 0.035$. As expected from the results shown in Fig. 1, the sensitivity is lower than the sensitivity of the single polarization measurements by approximately one order of magnitude. Non-linearity is also increased. The values for $a_{\Delta f}$ and $b_{\Delta f}$ found here, will be used in Section 5.1 to relate the measured ΔA to rain rate.

2.2. Microwave radiation and humidity

2.2.1. Attenuation

Besides precipitation, absolute humidity can be another major source of attenuation, especially at or close to the water vapor resonance frequency of 22.235 GHz. For a detailed

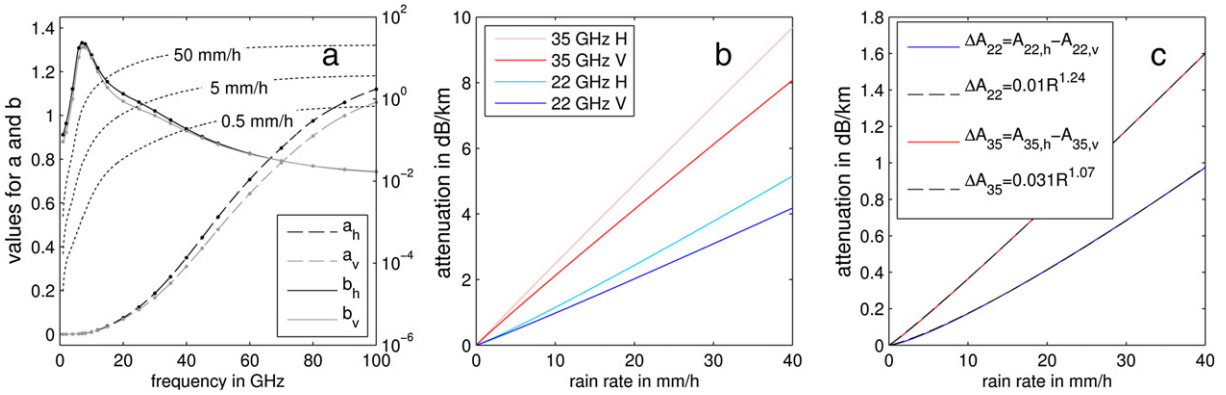

Fig. 2. (a) Values of a and b from ITU (2003) and the resulting attenuation for different rain rates (dotted lines). (b) Resulting attenuation for 22 GHz and 35 GHz for horizontal and vertical polarization depending on rain rate. (c) Resulting differential attenuation and power law fit obtained by non-linear least square fitting.

Table 2
The values of a and b used in the power law relation of A–R and ΔA–R (see Eqs. (6) and (8)). Values for A are taken from ITU (2003). Values for ΔA are obtained from the power law fit shown in Fig. 2c.

Frequency in GHz	a_h	a_v	a_Δ	b_h	b_v	b_Δ
34.8	0.260	0.230	0.031	0.981	0.964	1.070
22.235	0.096	0.088	0.010	1.081	1.048	1.240

calculation of the attenuation A_q in dB/km caused by the absolute humidity, depending on temperature T, pressure P and the used frequency, refer to Liebe (1989) and ITU (2001). By inversion of the relation of A_q given in ITU (2001), q in g/m^3 derived from a measured attenuation at 22.235 GHz can be approximated by

$$q = \left(-2 \times 10^{-5} P + 0.042\right)^{-1} A_q \tag{9}$$

with P being air pressure in mbar. This approximations is within 3% deviation of the original relation for values of P ranging from 900 mbar to 1000 mbar and T ranging from −10 °C to 30 °C. The approximation neglects any temperature dependency because it is marginal in our region of interest. At a typical pressure P of 950 mbar in the region studied, a change in absolute humidity of 1 g/m^3 results in a change of attenuation by 0.023 dB/km.

2.2.2. Phase delay

For path length of only few kilometers the attenuation due to humidity will be small. Thus it could easily be masked by fluctuations stemming from other sources (e.g. mechanical deflection of antennas, system drifts) or would not reach the detection limits of measurement systems. A more sensitive way to retrieve absolute humidity information is to use measurements of phase delay, where available. Phase delay is linearly related to the speed of propagation determined by the refractive index n, which in turn depends mainly on atmospheric pressure, temperature and humidity.

A change in the phase $\Delta\Phi$ is related to a change of the refractive index Δn by the equation

$$\Delta\phi = \frac{2\pi f r}{c} \Delta n \tag{10}$$

with f being the frequency in GHz, r the path length in m, and c the speed of light in vacuum. In the case of electromagnetic wave propagation through the atmosphere, deviations of the refractive index from 1 are very small. Hence the refractivity

$$N = (n-1) \times 10^6 \tag{11}$$

is defined as a magnification of this deviation, which, using Eq. (10), can be written as

$$N = N_0 + 10^6 \times \frac{\Delta\phi c}{2\,\pi f\, r} \tag{12}$$

with an initial refractivity N_0.

Following Bean and Dutton (1968) effects of atmospheric changes are related to refractivity with

$$N = 77.6 \frac{P}{T_k} + 3.73 \times 10^5 \frac{e}{T_k^2} \tag{13}$$

where P is the pressure in mbar, T_k the temperature in K and e the water vapor pressure. Using the relation

$$e = \frac{q\, T_k\, R}{M} \tag{14}$$

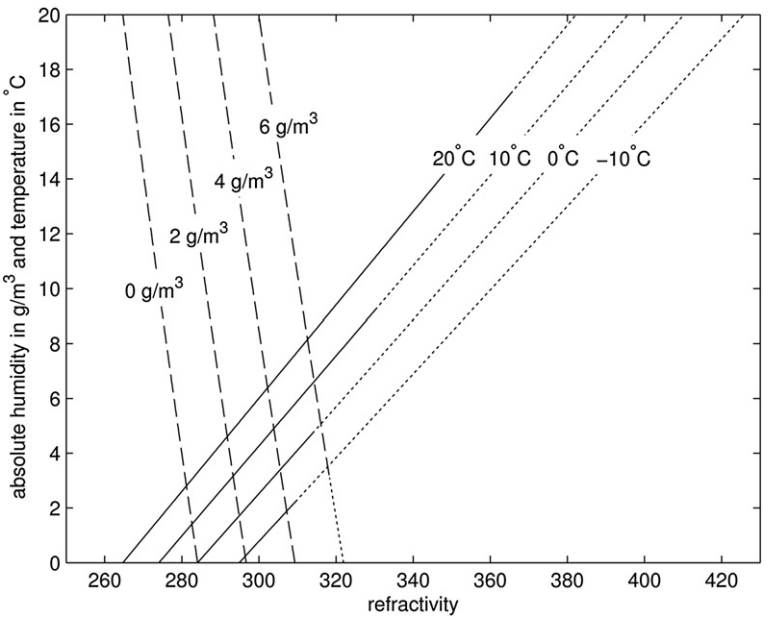

Fig. 3. Relation of refractivity to values of absolute humidity and temperature. The dotted lines indicate where a relative humidity exceeds 100%.

Eq. (13) can be write as

$$N = 77.6\frac{P}{T_k} + 3.73 \times 10^5 \frac{q\,R}{T_k M} \tag{15}$$

with the gas constant $R = 8.314472 \times 10^{-2}$ mbar m^3 mol^{-1} K^{-1} and the molar weight of water $M = 18.02$ g mol^{-1}. The resulting dependence of N on q and T is illustrated in Fig. 3. Changes in P are not considered in the plot, because they are negligible for the common pressure ranges of 900 to 1000 mbar.

It indicates that the impact of changes in absolute humidity by 1 g/m^3 is around six times larger than the impact of a temperature change by 1 °C. It is noted though, that during cold weather, when water vapor saturation is already reached at low absolute humidity values, e.g. ≈2 g/m^3 at −10 °C, the magnitude of temperature changes can easily exceed the changes by absolute humidity. Whereas during warm weather conditions with absolute humidity reaching high values, e.g. $\approx 30\frac{g}{m^3}$ at 30 °C, N is mainly governed by absolute humidity.

Fig. 4 illustrates such a situation. The course of the calculated refractivity, in particular the fluctuations on short time scales, mimic the course of the values of absolute humidity. Furthermore, it can also be seen, that temperature is a more continuous quantity than humidity. This is confirmed by autocorrelation analysis (not shown here) which yields a smaller correlation of humidity compared to temperature up to a lag of 1 h. Accordingly, temperature can be assumed to be less variable in space and time than humidity. Temperature sinks and sources are affected less by the heterogeneity of vegetation and soil. We conclude that it is reasonable to interpolate point measurements of T to correct the calculation of absolute humidity retrieved by means of phase delay measurements along a path of several kilometers.

3. Transmission experiment

3.1. Requirements

The system's frequencies had to be within the frequency band commonly used for commercial microwave communication link networks (10 GHz to 40 GHz), to allow transferability to investigations carried out with data from these networks. Additional requirements were that horizontal and vertical polarization measurements are performed simultaneously and stable phase information has to be delivered. Path length must be kept short at around ≈1 km to minimize the variability of precipitation along the path, and still keep the magnitude of expected attenuation high enough for detection. In addition everything had to fit into a reasonably small weatherproof housing to provide flexibility in system deployment.

The mentioned requirements result in a system principle equivalent to a dual frequency dual linearly polarized pulse radar using a trihedral corner reflector as fixed target. This monostatic configuration is necessary to provide stable phase information, which is not available in bistatic systems due to independent transmitter and receiver source drifts. Since there is only one active element, the monostatic system has the advantage of easy field deployment where power supply and internet connection are not always available. However, discrimination between transmitted (reflected by the trihedral reflector) and unwanted backscattered (directly from precipitation anywhere along the path) radiation is necessary (Ruf et al., 1996). This is accomplished by range gating the signal from the trihedral with a pulsed transmitter and receiver. With the possibility of humidity measurements at 22.235 GHz, this frequency along with 34.8 GHz (where low dependency on the DSD is expected) is selected.

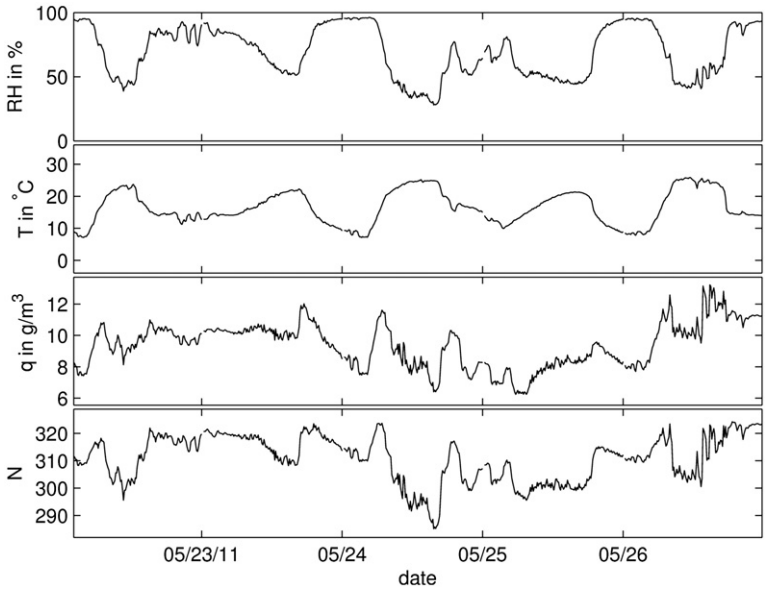

Fig. 4. Example of calculated refractivity N from temperature T, absolute humidity q and pressure P (not shown) recorded by the weather station described in Section 4.

3.2. Technical specifications

3.2.1. HF-system

The systems for both frequencies are similar and share the same 100 MHz crystal oscillator as reference source and operate simultaneously. The reference synchronizes a phase locked oscillator (PLO), whose output is converted up and split into the upper and lower sideband. These are then multiplied to provide the high frequency (HF) output and the reference signal for down conversion in the receiver stage. The multiplier provides an output power of ≈ 20 dBm. The PIN switch used for pulse generation is situated before the multipliers to preserve better isolation. To keep the system as compact as possible only one horn lens antenna per frequency, each with an aperture of 23 cm, is used for both transmission and reception. Polarization is altered by a ferrite polarizer. The transmitter (Tx) and receiver (Rx) chain are connected via a ferrite circulator and two additional PIN-switches (fast PIN-diode based switches) to the antenna to optimize isolation of the Tx from the Rx unit. The aforementioned lower sideband is used in Rx to down convert the output of the receiver low-noise amplifier (LNA), which is subsequently down-converted by an in-phase and quadrature (I/Q) mixer to provide the baseband I/Q outputs. Fig. 5 shows a simplified block diagram for the complete microwave system.

The system's pulse repetition frequency (PRF) is fundamentally determined by the total path length. To exclude two way echoes, the pulse repetition time (PRT) should to be at least twice the round trip time of a pulse reflected by the reflector. With the trihedral reflector at a distance of 660 m we thus have to use a PRF < 100 kHz. A further constrain of the system's PRF is the settling time of the ferrite polarizers. It is of importance because the system operates with alternating polarizations to perform quasi-simultaneous measurements for both polarizations. The high inductance of the polarizer coils of several mH results in a settling time between 20 μs and 35 μs until reaching a stable cross-polarization state (time may differ depending on polarizer and polarization state). A safe PRT thus is 40 μs. Hence, we set the system's standard PRF to 25 kHz. An overview of the basic system operating characteristics is given in Table 3.

Table 3
System operating characteristics.

	34.8 GHz	22.235 GHz
Antenna gain	36 dBi	32 dBi
3 dB beam width	2.4	4.2
Trihedral RCS	41 dBsm	36 dBsm
Tx power	18 dBm	16 dBm
Noise figure	10 dB	8 dB
PRF	25 kHz	25 kHz
Pol settling time	35 μs	35 μs
Pulse width	Min 100 ns	Min 100 ns
Two-way path length	1320 m	1320 m

3.2.2. Timing control and DAQ system

To keep the instrument enclosure as small as possible the timing generator and data acquisition (DAQ) system were tailored to the needs of the experiment. An embedded Linux operating system running on a small singleboard computer (SBC) provides a user interface via SSH remote login and also

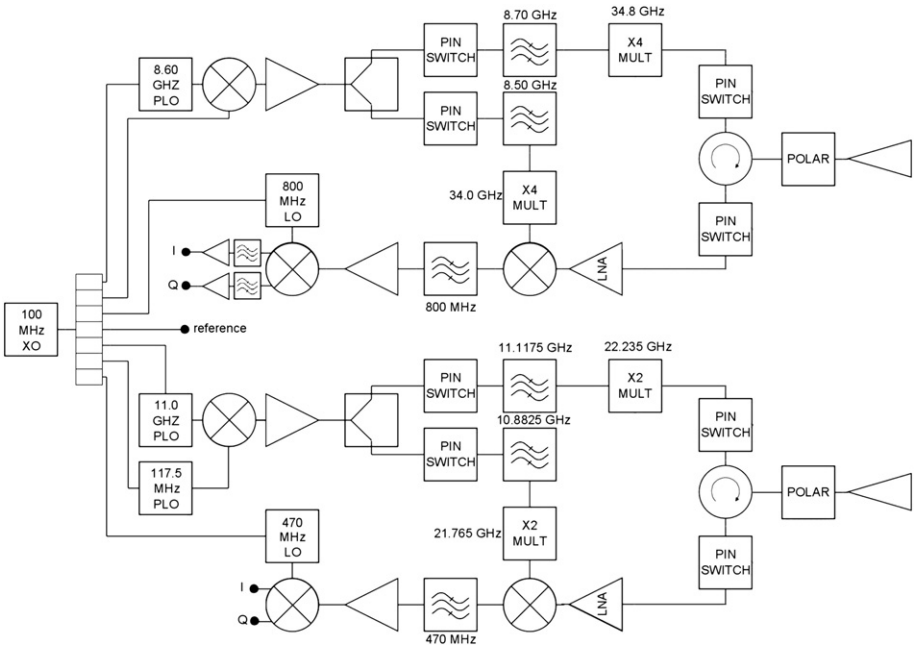

Fig. 5. Block diagram of the high frequency setup for both the 35 GHz and the 22 GHz systems.

handles the data transfer to a database server. Via High Speed USB, the SBC connects to a micro-controller (μC) on a printed circuit board (PCB) holding all other components of the control-system. On the PCB, the μC interfaces an ADC via a parallel bus and has an I2C-bus (a two wire serial bus) to connect to thermostats for the heating control and a complex programmable logic device (CPLD) which generates the pulse controlling the Tx and Rx switches. The ADC simultaneously samples four channels (I and Q for both frequencies) with a 12 bit resolution and passes the data on to the μC which continuously streams it to the SBC with a transfer rate of 1.2 MBit/s for a PRF of 25 kHz. The track & hold of the ADC is triggered by the pulse generator running on the CPLD controlling the switches of the HF system. Pulse width, delay for the receiver stage and PRF can be chosen and altered in 10 ns steps. The minimal values for pulse width, however, are determined by the rise and fall time of the switches. A schematic of the DAQ and control system is given in Fig. 6.

The timing control system allows different modes of operation. All data used in this work was acquired using the averaging mode with a pulse width of 200 ns. The averaging mode takes 32 continuous samples of the raw I and Q data sampled at 25 kHz and stores their average. This is done continuously every 50 ms, resulting in a sampling rate of 20 Hz. In this mode the accuracy of the received signal amplitude measurements is 0.1 dB for both frequencies and both polarization. However, attenuation measurements in the field are subject to larger fluctuations (up to 1 dB) due to tower movement and changing ground reflection properties.

4. Test site and equipment

The system is installed at the TERENO pre-alpine hydrometeorological test site in Fendt (47°49′59″N, 11°03′40″E, 600 m a.s.l.), about 50 km south of Munich, Germany. The mean annual precipitation is approximately 1100 mm, with a maximum of 200 mm per month observed in June and July. Mean annual temperature is around 8 °C, with high likeliness of snow fall during the winter months. An overview of the test site with detailed locations of all devices is displayed in Fig. 7.

4.1. Laser disdrometer

At the site, a *Thies* Laser Disdrometer mounted at the Tx/Rx tower 10 m above the ground provides minute resolution drop diameter and drop velocity data. To discriminate the different precipitation types (rain, hail, graupel, snow) and false detections by the disdrometer (margin fallers and splashed drops) in this data, we adopted the approach presented by Friedrich et al. (2012). It uses the theoretical fall velocities for the different precipitation types with corresponding error margins to classify precipitation types for each diameter–velocity combination. For their data, recorded by a PARSIVEL disdrometer, they used a 60% error margin for the terminal velocity of rain drops. The successful use of a 40% margin is also reported, though. For our data we use a 50% margin for the terminal velocity of rain drops, resulting in less than 5% of rain amount being removed due to excluded drops (margin fallers, splashed drops, uncategorized). The mask applied for classification is shown in Fig. 8.

4.2. Weather station

In the vicinity of the reflector tower, a Vaisala WXT520 weather station is installed at an Eddy-Correlation (EC) flux measurement tower at 2 m above the ground. It provides ten minute averages of temperature, humidity, pressure and rain rate.

Absolute humidity q is calculated from the measured temperature T_k in Kelvin and relative humidity (RH) in % using

$$q = \frac{e\,M}{R\,T_k} \tag{16}$$

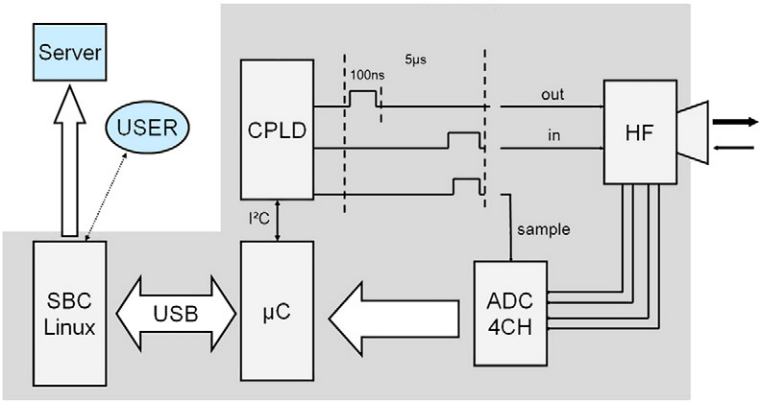

Fig. 6. A schematic of the data acquisition and pulse control system. The gray shaded area indicates the weatherproof housing. HF denotes the high frequency hardware shown in Fig. 5.

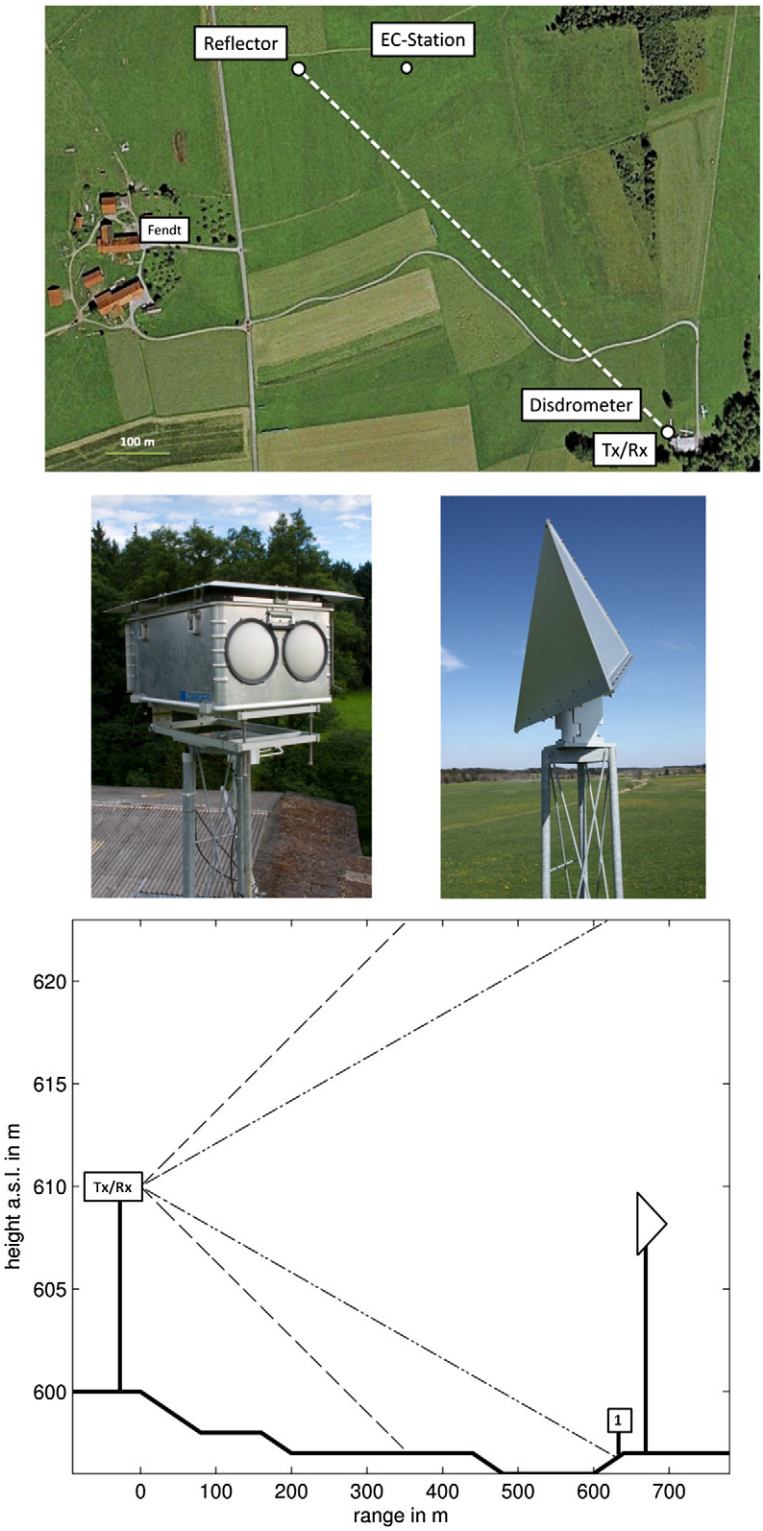

Fig. 7. An overview of the TERENO test site in Fendt with the locations of the Tx/Rx towers and the EC-station. In the middle, pictures of the Tx/Rx box and of the reflector in the field are given. In the height profile the 3 dB beam width of the 22 GHz system (dashed line) and the 35 GHz system (dash-dotted line) is depicted. The WXT520 weather station is located at the EC-station, shown as (1) in the height profile plot.

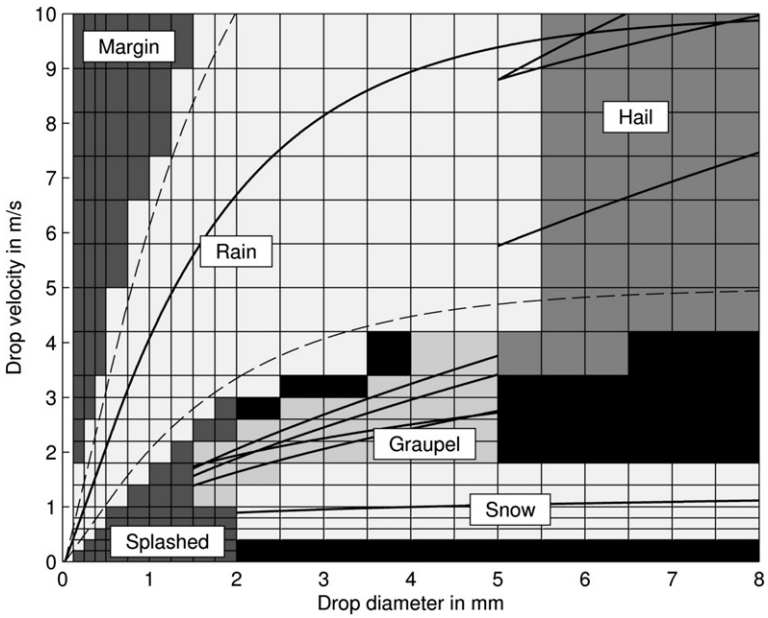

Fig. 8. The mask used to discriminate the different precipitation types in the raw drop and velocity data recorded by the disdrometer. The black lines give theoretical terminal velocities for the different precipitation types. The dashed line is the 50% error margin used to define the corridor for the drops classified as rain. For details please refer to Friedrich et al. (2012).

and the relation for water vapor pressure

$$e = \frac{RH}{100} 611.2 exp\left(\frac{17.67(T_k - 273.15)}{T_k - 29.65}\right). \quad (17)$$

4.3. Transmission experiment setup

Both the transmit/receive box and the trihedral reflector were installed on the top of 10 m towers. The 660 m path between the towers leads over flat grassland with an unobstructed first Fresnel zone. As can be seen from Fig. 7 the 3 dB beam width of the 22 GHz system however hits the ground half way to the reflector, resulting in potential fluctuations due to multipath propagation. The 35 GHz system with its narrower beam is less prone to this effect.

5. First results

5.1. Precipitation

5.1.1. Rain event May 2nd 2011

As a first case study a strong isolated rain event on May 2nd 2011 is chosen. The duration of 20 minutes and the intensity with rainrates up to 30 mm/h indicate a typical convective type of rain event. The disdrometer measurements shown in Fig. 9-b1 also indicate that a significant part of the precipitation particles has been classified as snow and hail. For the following analysis we neglect the contribution of hail since only little can be known about the actual shape, density and the water coating of the hail stones from the disdrometer measurements. These parameters however, are necessary to model their scattering characteristics (Borowska et al., 2011). The snow particles are also neglected since attenuation by snowflakes (assumed that they are not coated with water) is very low.

Data from the experiment which is recorded at 20 Hz is averaged to 1 Hz and shown in the left column of Fig. 9. As expected, the received signal level (RSL) displayed in Fig. 9-a1 mimics the time course of the rain event recorded by the disdrometer (shown in Fig. 9d). Due to the higher sampling rate (1 Hz for the RSL compared to 1 record every minute for the disdrometer) the RSL data reveals in much more detail the rain intensity fluctuations on short time scales.

For the RSL based calculation of rain rates, attenuation values are necessary, for which a reference baseline value has to be assumed. Here, the mean value of RSL before the rain event was chosen. For continuous operation, dynamic baseline algorithms are more appropriate. They cope with the long term drift and fluctuations of RSL (Rahimi et al., 2003; Goldshtein et al., 2009; Overeem et al., 2011; Schleiss and Berne, 2010; Chwala et al., 2012).

When comparing measured A and ΔA to the values calculated from the DSD recorded by the disdrometer (Fig. 9-b2 and b3) and to values calculated for a Marshall–Palmer DSD based on R as measured by the disdrometer (Fig. 9-c2 and c3), deviations can be observed. In particular the behavior of $A_{22,h}$ and hence ΔA_{22} can not be reproduced when using a fixed DSD. This can also be seen in row 4 of Fig. 9 where the ratio $\Delta A/A_h$ is shown. Comparison with the median volume diameter D_0 of the measured DSD, shown in Fig. 9-c1, suggests a dependence of $\Delta A/A_h$ on D_0. This can be explained by the fact that the same attenuation level can be generated by different DSDs. With increasing D_0, ΔA will however increase due to the more pronounced asymmetry of the larger drops. As was shown in Section 2.1.1 and Fig. 1, in

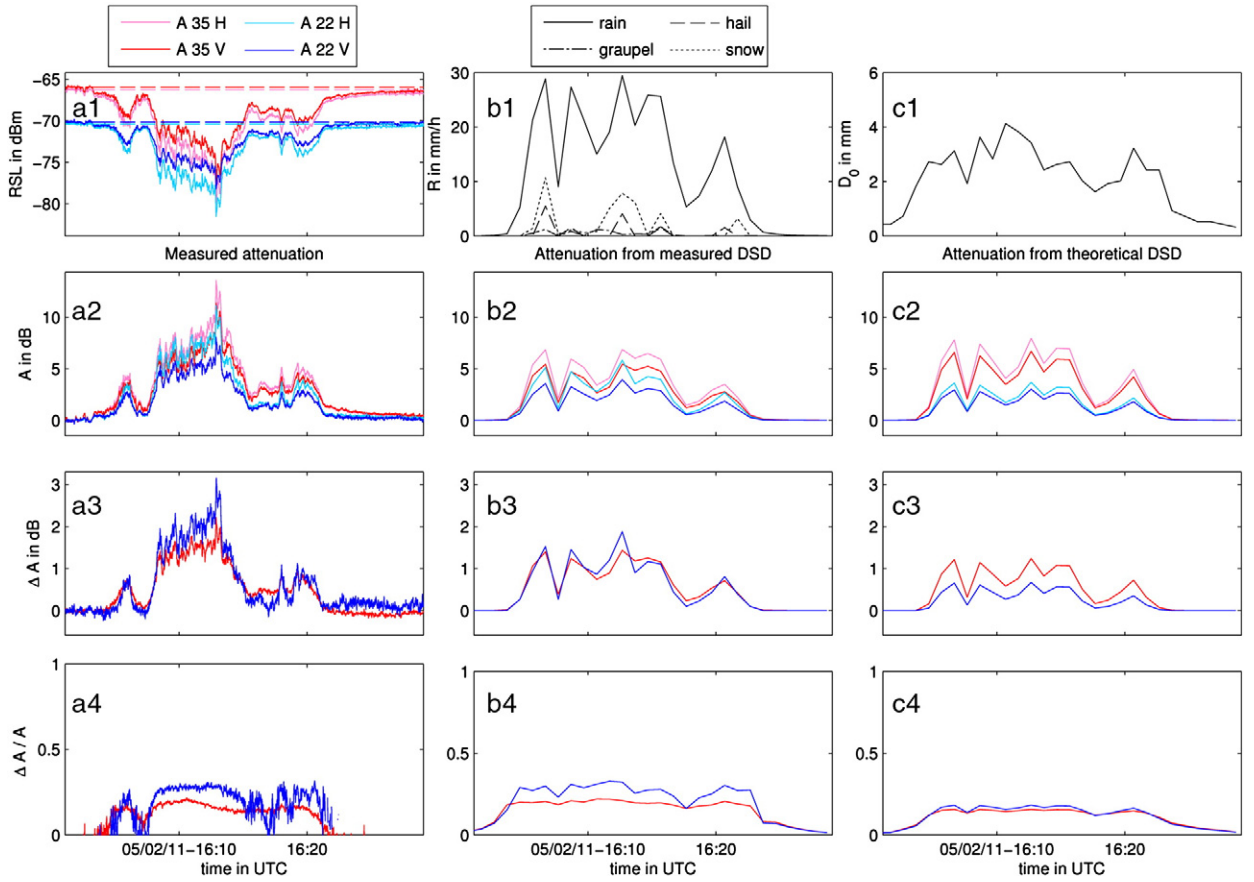

Fig. 9. Time series for rain event on May 2nd 2011. Data from the transmission experiment is sampled at 1 Hz. Disdrometer data has minute resolution. Plot (a1) shows the received signal level (RSL). Plot (b1) shows the rain rates for different precipitation types derived from the disdrometer raw data employing the mask shown in Fig. 8. Plot (c1) shows the median volume drop diameter for rain. Plots in rows 2, 3 and 4 show the derived attenuation A, differential attenuation ΔA and $\Delta A/A$ derived from the RSL (plots in column a), from the DSD measured by the disdrometer (plots in column b) and from a Marshall–Palmer DSD according to the rain rate measured by the disdrometer. Note that values for $A < 0.5$ dB are not shown in plot (a4) since the fraction diverges when A approaches 0.

particular $C_{\mathrm{ext},22,h}$ increases in the presence of large drops ($D > 4$ mm).

For a direct comparison of measured and calculated A and ΔA, the first two rows in the plot matrix in Fig. 10 show the minute averages of data from the experiment and the disdrometer. The black lines give values calculated for the different theoretical DSDs from Table 1. The thick dashed black line uses the power law relation given in Eq. (6) with values of a and b according to Table 2. As expected from the findings in Section 2.1.1 the spread, and hence the dependence on the choice of the theoretical DSD, is smaller for 35 GHz than for 22 GHz. The measured data also exhibits this behavior.

In general the disdrometer data seems to have larger values of $\Delta A/A$. This can be explained by two effects.

First, the DSD used for the calculation of A and ΔA only contains drops classified as rain. Hail is neglected. For the attenuation measurements however, hail contributes to A and ΔA. If this contribution would be removed, A and ΔA would change. Since the axial asymmetry of hail stones is smaller than that of large rain drops (Knight, 1986), removing hail from the signal would decrease A while $\Delta A/A$ increases. This would result in a better alignment of the data from the experiment and the data from the disdrometer.

Second, the effect of wet antenna could lead to an overestimation of A measured by the experiment. The values for low $\Delta A/A$ in Fig. 10-a2 and b2 indicate that the antenna must have been wet, since, $\Delta A = 0$ indicates that no rain is present. If A is still significantly larger than zero, this attenuation is likely to stem from the water remaining on the slowly drying antenna. Future research will show if the resulting deviations from the theoretical curves can be used to detect wet antenna attenuation and remove it in post-processing.

If there is no DSD data available, rain rates have to be derived from measured attenuation using the A–R power law relation given in Eq. (6). This relation assumes a fixed DSD for each rain rate. Deviations of that DSD will thus lead to errors in the derived rain rate. We study this effect of a changing DSD by comparing observed attenuation A_{obs} from the experiment to attenuation A_{calc} calculated from the measured DSD provided by the disdrometer. From A_{obs} a rain rate R_{calc} is calculated using the power law from Eq. (6) with the values from Table 2. R_{calc} is then compared to the rain rate R_{obs} derived from the disdrometer DSD data. When comparing the correlation

between A_{obs} and A_{calc} to the correlation between R_{calc} and R_{obs}, a decrease should be observable, which should be more pronounced if the dependence of the A–R relation on the DSD is higher.

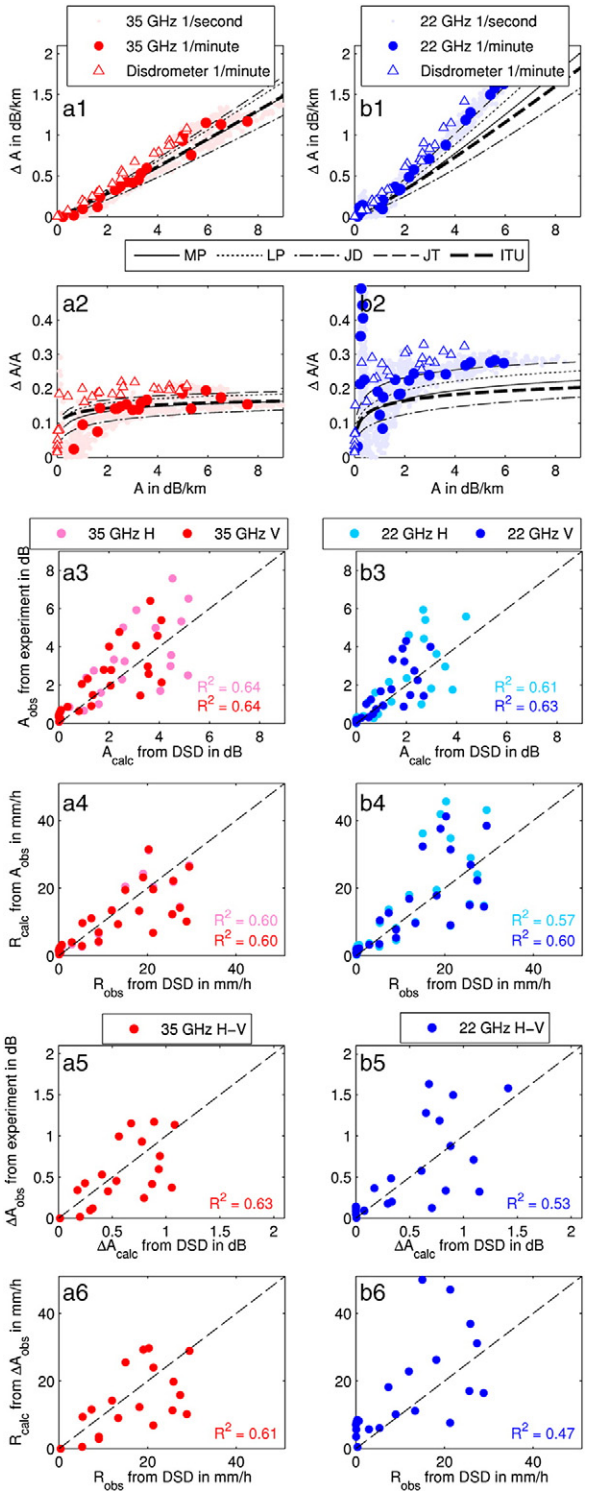

The plots in rows 3 to 6 of Fig. 10 show this comparison for A and ΔA. The Pearson correlation coefficient confirms the above mentioned expectation. It decreases when rain rates are derived from measured attenuation with a fixed A–R power law.

5.1.2. Rain event March 30th 2011

As second example a medium rain event on March 30th 2011 is chosen. Even though it is less intense than the event studied in the last section its isolated nature and short duration indicate a convective type rainfall. The large median volume diameter D_0, shown in Fig. 11, at the onset confirms this indication. Similar to the analysis in Fig. 9, the large D_0 is reflected in the differential signals, in particular in ΔA_{22}. The fixed Marshall–Palmer DSD cannot reproduce that.

In the scatter plots in rows 1 and 2 of Fig. 12 both, the measured attenuation values and the ones calculated from the disdrometer, indicate a significant deviation from the theoretical DSDs towards large rain drops. Again, wet antenna attenuation and its slow recovery can be observed, most pronounced in Fig. 12-a2. The presence of comparatively large drops for the given rain rates also explains the results of the correlation analysis presented in the scatter plots in rows 3 to 6 of Fig. 12. Similar to the result shown in Fig. 10, the correlation decreases when going from the comparison of A to the comparison of R. In this case however, the decrease for $A_{22,\,h}$ and ΔA_{22} is significant. An explanation might be the strong deviation of the present DSD from the theoretical ones, as indicated in Fig. 12-a2 and b2.

Concluding from the results shown in Figs. 9 and 11 the measured data is consistent with the theoretical findings from Section 2.1.1. The almost linear relation between the integrands of A and R (see Eqs. (1) and (3)) at 35 GHz results in a low dependence of the A–R relation on the DSD. This relation can be approximated well by the power law from Eq. (6) using the ITU values given in Table 2. At 22 GHz and horizontal polarization or when using data from differential measurements, the ITU power law seems not to be able to reproduce the correct attenuation values.

5.2. Humidity estimation from May 18th 2011 till May 26th 2011

To study the relation between the measured phase delay and the absolute humidity a period of warm weather conditions in May 2011 is selected. Phase information is taken from the 22 GHz and 35 GHz system, running at 20 Hz sampling rate. Prior to averaging to 1 Hz data, the phase

Fig. 10. Scatter plots of the data from the rain event on May 2nd 2011 shown in Fig. 9. Plot (a1) shows the values of attenuation A and differential attenuation ΔA, from 1 Hz attenuation measurements of the 35 GHz system, from minute averages of this 1 Hz data and the attenuation values calculated from DSDs measured by the disdrometer. Plot (a2) shows the same data in a different representation. Plot (a3) shows A_{obs} observed by the experiment and A_{calc} calculated from the DSD. In plot (a4) R_{calc} is the rain rate calculated from A_{obs} employing the power law relation given in Eq. (6). R_{obs} is derived from the DSD. Plots (a5) and (a6) are similar to (a3) and (a4) showing values for ΔA. Plots in column (b) refer to data from the 22 GHz system. Note that the divergence of $\Delta A/A$ in plot (b2) is due to the fluctuations of A close to zero.

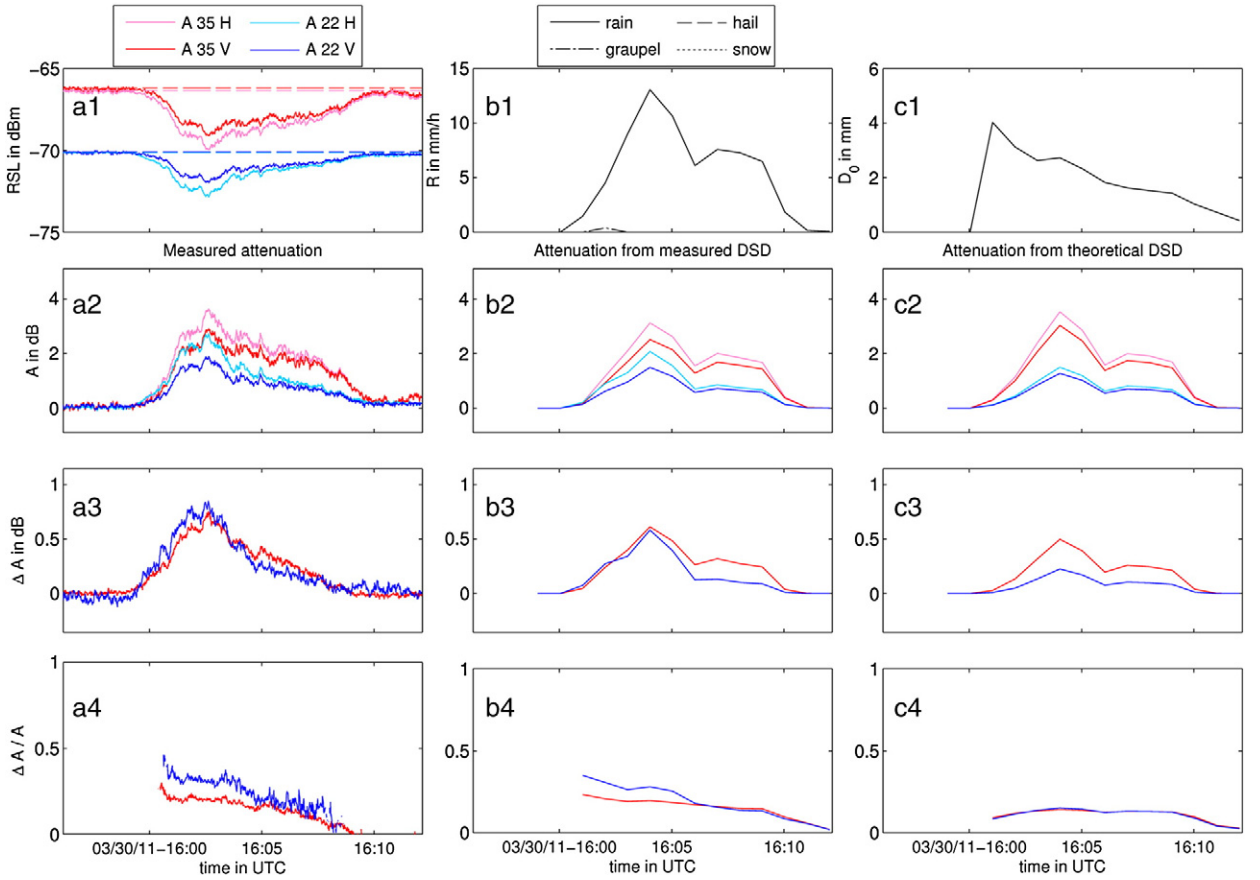

Fig. 11. Same as Fig. 9 for a rain event on March 30th 2011. DSD data from the disdrometer before 15:59 UTC is missing because the exported raw data was corrupted. Precipitation intensity values given by the disdrometer's internal processing yielded no precipitation, though.

skipping over every 2π, has to be unwrapped. Strong wind causes tower oscillations at 4 Hz which tend to corrupt unwrapping at lower sampling rates.

From the unwrapped phase, refractivity is calculated using Eq. (12) with the offset N_0 calculated from weather station data at noon of the starting day of the phase time series. Using Eq. (15) with temperature and pressure data from the weather station interpolated to 1 Hz, absolute humidity values are derived. The resulting time series together with an uncorrected time series using fixed values T = 15 °C and P = 953 mbar is shown in Fig. 13. As mentioned in Section 2.2.2 and also observable here, temperature and pressure are changing on a slower temporal scale than humidity. However, comparing the corrected with uncorrected data for a longer time interval, e.g. during the course of a day, the influence particularly of the high diurnal temperature variations on the derived absolute humidity is visible. The corrected data align well with the station data. This is also confirmed by the scatter plots in Fig. 14 and the reasonable Pearson correlation coefficient of $R^2 = 0.77$ and $R^2 = 0.79$ for both the 35 GHz and 22 GHz system.

The observable deviations seem to follow a pattern. On several days (e.g. on May 19th at around 06:00 UTC) sharp decreases with sudden recoveries occur in the morning hours. Cross-checking of these incidents with radiation data (not shown here) from the weather station at the eddy correlation tower indicates that they are appearing only during days with high solar radiation. It is thus very likely that the fast decreases with subsequent recovery stem from mechanical deflection of the towers caused by one-sided heating due to solar radiation at sunrise and sunset. During night time the phase derived humidity is often overestimated. This might be explained by the location of the test site. It is situated in a wide flat valley, where the high soil moisture of the meadows often leads to fog when the atmosphere is stable. Thus a temperature and moisture gradient could lead to considerable differences between the met station measurements at 2 m and the measurements of the phase delay 10 m above the ground.

The deviations occurring on a smaller (sub-minute) temporal scale, and with pronounced fluctuations during daytime and maximum amplitudes around noon, originate from fluctuations of the refractive index caused by evaporation. This is an effect that is exploited in remote sensing the latent heat flux using microwave and optical scintillometers (Meijninger et al., 2006; Leijnse et al., 2007a). With these instruments, amplitude fluctuations are evaluated. With the additional phase derived humidity measurements shown here, new insight into boundary layer processes may be possible.

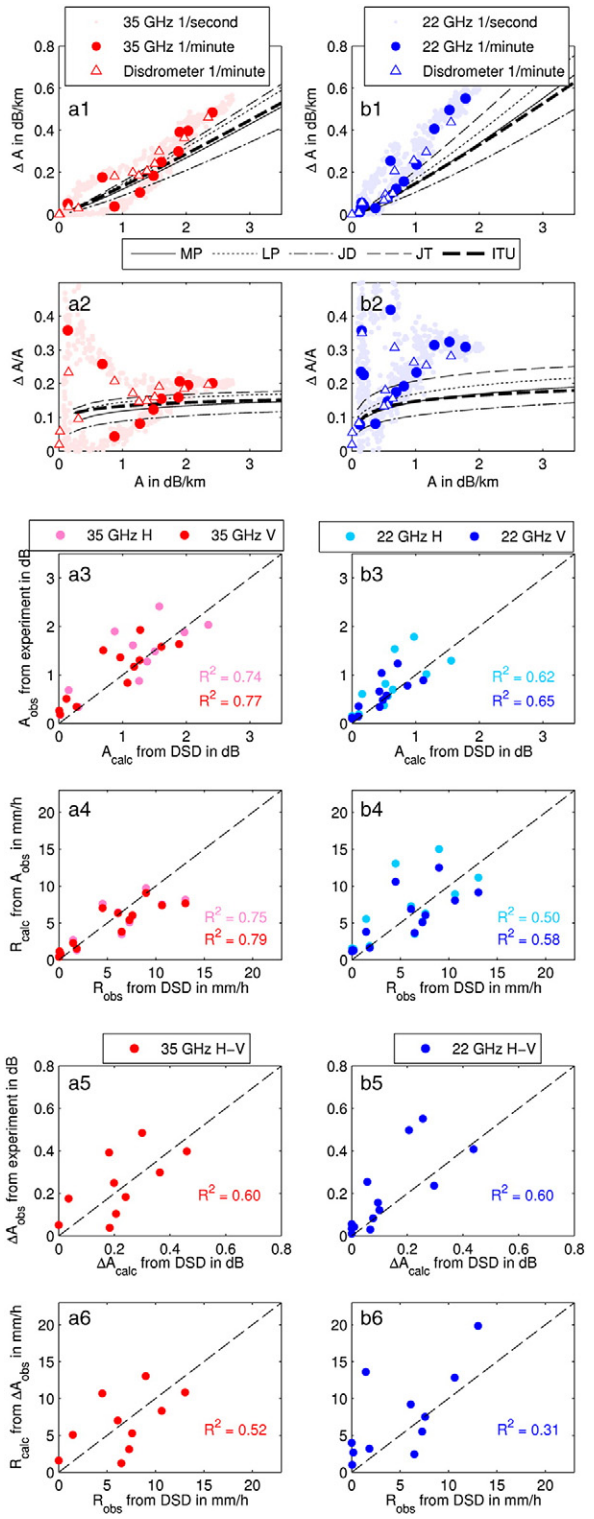

Fig. 12. Scatter plots of the data from the rain event on March 30th 2011. Plot structure is the same as in Fig. 10. The divergence of $\Delta A/A$ in plot (b2) is due to the fluctuations of A close to zero.

6. Conclusion and outlook

We have designed and built up a dual frequency dual linearly polarized monostatic transmission experiment which is operated over a 660 m path at the hydrometeorological TERENO pre-alpine test site in Southern Germany. Three test cases were examined analyzing attenuation and phase delay data.

Six different attenuation measures (horizontal and vertical polarization, 34.8 GHz and 22.235 GHz, and the differential attenuation between horizontal and vertical polarization) were analyzed. Due to the relatively short path length, noise can mask the signal attenuation for weak rain events. This is in particular true for measurements of differential attenuation, which are less sensitive than measurements of specific attenuation. The analysis was hence focused on stronger convective events. The ratio of attenuation to differential attenuation $\Delta A/A$ was found to be sensitive to changes of the median volume diameter. Comparison with DSD data simultaneously obtained by a disdrometer at the test site showed reasonable agreement.

Using the disdrometer data, the effect of a variable DSD on the performance of the A–R power law fit was studied. It was shown that, as described by theory, the effect is low at 35 GHz and increases for 22 GHz and the differential measurements.

Phase delay measurements were used to derive refractivity values. Transformed to absolute humidity these data were consistent with data obtained at the weather station in the vicinity. The scale investigated by the experiment is in the same order of magnitude as the resolution of recent atmospheric models. In the future this may provide a new possibility to initialize and validate these models.

Further examination of the spatial variability of humidity and its impact on the line integrated measurement is mandatory to check the accuracy of the phase derived humidity. Therefore installing additional humidity loggers as supplemental ground truth will be considered.

For the analysis of precipitation, it is also planned to install rain gauges or disdrometers for ground truthing along the path. A first next step in evaluating the attenuation data might be the implementation of the methods proposed for line integrated DSD retrieval, using two frequencies or two polarizations (Rincon and Lang, 2002; Berne and Schleiss, 2009). Having both, two frequencies and two polarizations available, may offer an even more detailed analysis of the DSD. In addition, measurements of the differential propagation phase, which is a further independent quantity sensitive to precipitation, could add to the robustness of the DSD estimation.

Furthermore, the 25 KHz raw data sampling mode will be used to study Doppler spectra, both in transmission and reflection. Their empirical analysis will be accompanied by a numerical model of microwave propagation through rain, simulating the interaction with each single drop, following (Hipp et al., 2011).

Acknowledgment

We thank the three anonymous reviewers for their constructive comments, which helped improving the quality of our paper. The authors also want to thank Michael Rožmann

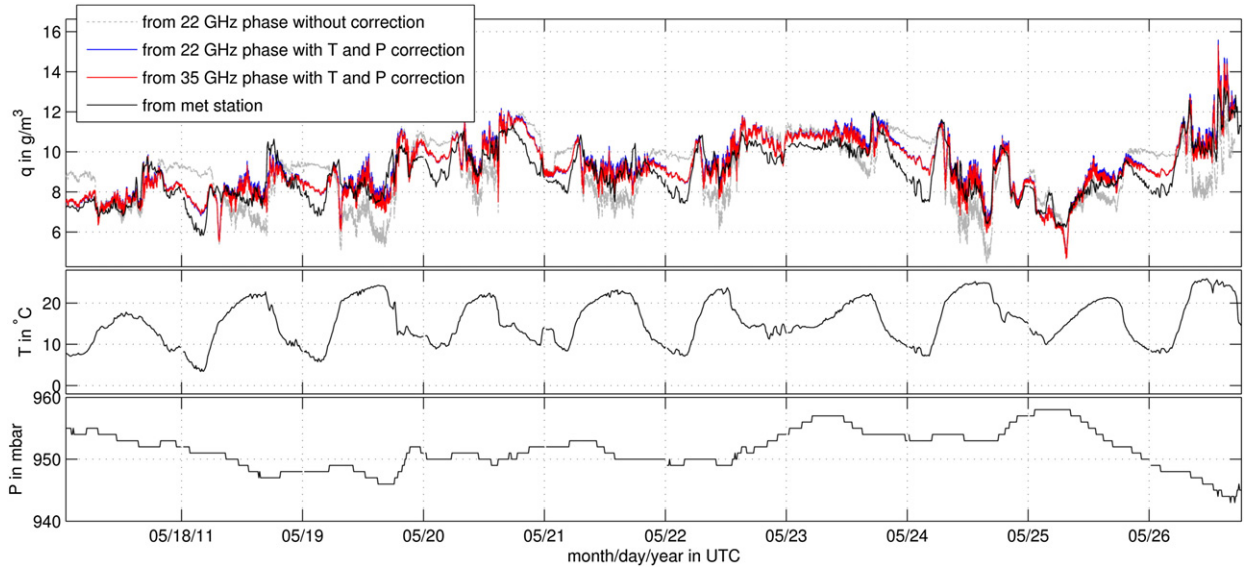

Fig. 13. Time series of absolute humidity derived from phase measurements of the 22 GHz and 35 GHz system. The 22 GHz data is shown with and without correcting the results using temperature *T* and pressure *P* from the meteorological station in the vicinity. The uncorrected data for the 35 GHz system would be similar and is not shown here.

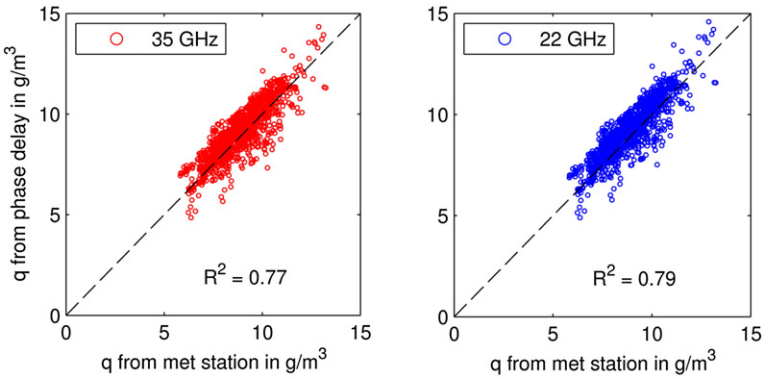

Fig. 14. Scatter plot of the time series shown in Fig. 13. Here 10 min averages of phase derived humidity values are used to be comparable to the 10 min averages provided by the met station.

and Jeffrey Paul for their good cooperation in developing the high frequency system. This work was funded by the Helmholtz Association of German Research Centres under grant VH-VI-314 (Regional Precipitation Observation by Cellular Network Microwave Attenuation and Application to Water Resources Management, PROCEMA). TERENO (http://www.tereno.net) infrastructure is also gratefully acknowledged.

References

Andrieu, H., Creutin, J.D., Delrieu, G., Faure, D., 1997. Use of a weather radar for the hydrology of a mountainous area. Part I: radar measurement interpretation. J. Hydrol. 193, 1–25.

Atlas, D., 1964. Advances in radar meteorology. Advances in Geophysics, 10. Academic Press, p. 385.

Atlas, D., Ulbrich, C.W., 1977. Path- and area-integrated rainfall measurement by microwave attenuation in the 1–3 cm band. J. Appl. Meteorol. 16, 1322–1331.

Aydin, K., Daisley, S., 2002. Relationships between rainfall rate and 35-GHz attenuation and differential attenuation: modeling the effects of raindrop size distribution, canting, and oscillation. IEEE Trans. Geosci. Remote Sens. 40, 2343–2352.

Bean, B.R., Dutton, E.J., 1968. Radio Meteorology. Dover Publications 435.

Beard, K.V., 1976. Terminal velocity and shape of cloud and precipitation drops aloft. J. Atmos. Sci. 33, 851–864.

Berne, A., Schleiss, M., 2009. Retrieval of the rain drop size distribution using telecommunication dual-polarization microwave links. 34th Conference on Radar Meteorology.

Bevis, M., Businger, S., Herring, T., Rocken, C., Anthes, R., Ware, R., 1992. GPS meteorology — remote sensing of atmospheric water vapor using the global positioning system. J. Geophys. Res. 97, 15787–15801.

Borowska, L., Ryzhkov, A., Zrnić, D., Simmer, C., Palmer, R., 2011. Attenuation and differential attenuation of 5-cm-wavelength radiation in melting hail. J. Appl. Meteorol. Climatol. 50, 59–76.

Chuang, C.C., Beard, K.V., 1990. A numerical model for the equilibrium shape of electrified raindrops. J. Atmos. Sci. 47, 1374–1389.

Chwala, C., Gmeiner, A., Qiu, W., Hipp, S., Nienaber, D., Siart, U., Eibert, T., Pohl, M., Seltmann, J., Fritz, J., Kunstmann, H., 2012. Precipitation observation using microwave backhaul links in the alpine and pre-alpine region of southern Germany. Hydrol. Earth Syst. Sci. 16, 2647–2661.

Cuccoli, F., Facheris, L., Tanelli, S., Giuli, D., 2001. Microwave attenuation measurements in satellite-ground links: the potential of spectral analysis for water vapor profiles retrieval. IEEE Trans. Geosci. Remote Sens. 39, 645–654.

David, N., Alpert, P., Messer, H., 2009. Technical note: novel method for water vapor monitoring using wireless communication networks measurements. Atmos. Chem. Phys. 9, 2413–2418.

Fabry, F., Frush, C., Zawadzki, I., Kilambi, A., 1997. On the extraction of near-surface index of refraction using radar phase measurements from ground targets. J. Atmos. Ocean. Technol. 14, 978–987.
Friedrich, K., Kalina, E.A., Masters, F.J., Lopez, C.R., 2012. Drop-size distributions in thunderstorms measured by optical disdrometers during VORTEX2. Mon. Wea. Rev. 141, 1182–1203.
Goldshtein, O., Messer, H., Zinevich, A., 2009. Rain rate estimation using measurements from commercial telecommunications links. IEEE Trans. Signal Process. 57, 1616–1625.
Hazenberg, P., Leijnse, H., Uijlenhoet, R., 2011. Radar rainfall estimation of stratiform winter precipitation in the Belgian Ardennes. Water Resour. Res. 47, W02507.
Hipp, S., Siart, U., Chwala, C., Eibert, T., Kunstmann, H., 2011. Dynamic modelling of atmospheric microwave transmission for precipitation quantification using mie scattering. Antennas and Propagation (EUCAP), Proceedings of the 5th European Conference, pp. 3380–3383.
Holt, A., Kuznetsov, G., Rahimi, A., 2003. Comparison of the use of dual-frequency and single-frequency attenuation for the measurement of path-averaged rainfall along a microwave link. IEE Proc. Microwaves Antennas Propag. 150, 315–320.
ITU, 2001. ITU-R p. 676–9: Attenuation by Atmospheric Gases. International Telecommunication Union.
ITU, 2003. ITU-R p. 838–2: Specific Attenuation Model for Rain for Use in Prediction Methods. International Telecommunication Union.
Joss, J., Waldvogel, A., 1969. Raindrop size distribution and sampling size errors. J. Atmos. Sci. 26, 566–569.
Knight, N.C., 1986. Hailstone shape factor and its relation to radar interpretation of hail. J. Clim. Appl. Meteorol. 25, 1956–1958.
Laws, J.O., Parsons, D.A., 1943. The relation of raindrop-size to intensity. Trans. Am. Geophys. Union 24, 452–460.
Leijnse, H., Uijlenhoet, R., Stricker, J.N.M., 2007a. Hydrometeorological application of a microwave link: 1. evaporation. Water Resour. Res. 43, W04416.
Leijnse, H., Uijlenhoet, R., Stricker, J.N.M., 2007b. Hydrometeorological application of a microwave link: 2. precipitation. Water Resour. Res. 43, W04417.
Leijnse, H., Uijlenhoet, R., Stricker, J.N.M., 2007c. Rainfall measurement using radio links from cellular communication networks. Water Resour. Res. 43, W03201.
Liebe, H.J., 1989. MPM — An atmospheric millimeter-wave propagation model. Int. J. Infrared Millimeter Waves 10, 631–650.
Liebe, H.J., Hufford, G.A., Manabe, T., 1991. A model for the complex permittivity of water at frequencies below 1 THz. Int. J. Infrared Millimeter Waves 12, 659–675.
Marshall, J.S., Palmer, W.M.K., 1948. The distribution of raindrops with size. J. Meteorol. 5, 165–166.
Mätzler, C., Martin, L., 2003. Advanced Model of Extinction by Rain and Measurements at 38 and 94 GHz and in the Visible Range. IAP Research Report. University of Bern, Bern, Switzerland.
Meijninger, W., Beyrich, F., Lüdi, A., Kohsiek, W., Bruin, H., 2006. Scintillometer-based turbulent fluxes of sensible and latent heat over a heterogeneous land surface — a contribution to Litfass-2003. Boundary-Layer Meteorol. 121, 89–110.
Messer, H., Zinevich, A., Alpert, P., 2006. Environmental monitoring by wireless communication networks. Science 312, 713.
Minda, H., Nakamura, K., 2005. High temporal resolution path-average rain gauge with 50-GHz band microwave. J. Atmos. Oceanic Technol. 22, 165–179.
Mishchenko, M.I., 2000. Calculation of the amplitude matrix for a nonspherical particle in a fixed orientation. Appl. Opt. 39, 1026–1031.
Mueller, G., 1946. Propagation of 6-millimeter waves. Proc. IRE 34, 181–183.
Nešpor, V., Sevruk, B., 1999. Estimation of wind-induced error of rainfall gauge measurements using a numerical simulation. J. Atmos. Oceanic Technol. 16, 450.
Olsen, R., Rogers, D., Hodge, D., 1978. The aRbrelation in the calculation of rain attenuation. IEEE Antennas Propag. 26, 318–329.
Overeem, A., Leijnse, H., Uijlenhoet, R., 2011. Measuring urban rainfall using microwave links from commercial cellular communication networks. Water Resour. Res. 47, W12505.
Pruppacher, H.R., Beard, K.V., 1970. A wind tunnel investigation of the internal circulation and shape of water drops falling at terminal velocity in air. Q. J. R. Meteorol. Soc. 96, 247–256.
Rahimi, A.R., Holt, A.R., Upton, G.J.G., Cummings, R.J., 2003. Use of dual-frequency microwave links for measuring path-averaged rainfall. J. Geophys. Res. 108 (D15), 4467.
Rincon, R.F., Lang, R.H., 2002. Microwave link dual-wavelength measurements of path-average attenuation for the estimation of drop size distributions and rainfall. IEEE Trans. Geosci. Remote Sens. 40, 760–770.
Roberts, R.D., Fabry, F., Kennedy, P.C., Nelson, E., Wilson, J.W., Rehak, N., Fritz, J., Chandrasekar, V., Braun, J., Juanzhen, S., et al., 2008. REFRACTT 2006: real-time retrieval of high-resolution, low-level moisture fields from operational NEXRAD and research radars. Bull. Am. Meteorol. Soc. 89, 1535–1548.
Ruf, C.S., Aydin, K., Mathur, S., Bobak, J.P., 1996. 35-GHz dual-polarization propagation link for rain-rate estimation. J. Atmos. Oceanic Technol. 13, 419–425.
Schleiss, M., Berne, A., 2010. Identification of dry and rainy periods using telecommunication microwave links. IEEE Geosci. Remote Sens. Lett. 7, 611–615.
Sevruk, B., Zahlavova, L., 1994. Classification system of precipitation gauge site exposure: evaluation and application. Int. J. Climatol. 14, 681–689.
Smith, D.R., Pumphry, M.E., Snow, J.T., 1986. A comparison of errors in objectively analyzed fields for uniform and nonuniform station distributions. J. Atmos. Oceanic Technol. 3, 84–97.
Stratton, J., 1930. The effect of rain and fog on the propagation of very short radio waves. Proc. Inst. Radio Eng. 18, 1064–1074.
Ulbrich, C.W., 1983. Natural variations in the analytical form of the raindrop size distribution. J. Clim. Appl. Meteorol. 22, 1764–1775.
Ulbrich, C.W., Lee, L.G., 1999. Rainfall measurement error by WSR-88D radars due to variations in Z–R law parameters and the radar constant. J. Atmos. Oceanic Technol. 16, 1017–1024.
Upton, G., Holt, A., Cummings, R., Rahimi, A., Goddard, J., 2005. Microwave links: the future for urban rainfall measurement? Atmos. Res. 77, 300–312.
Ware, R., Rocken, C., Exner, M., Feng, D., Herman, B., Gorbunov, M., Hardy, K., Kuo, Y., Meehan, T., Melbourne, W., 1996. GPS sounding of the atmosphere from low earth orbit: preliminary results. Bull. Am. Meteorol. Soc. 77, 19–40.
Waterman, P.C., 1971. Symmetry, unitarity, and geometry in electromagnetic scattering. Phys. Rev. D 3, 825.
Weckwerth, T.M., Pettet, C.R., Fabry, F., Park, S.J., LeMone, M.A., Wilson, J.W., 2005. Radar refractivity retrieval: validation and application to short-term forecasting. J. Appl. Meteorol. 44, 285–300.
Wolf, D.A.d, 2001. On the laws-parsons distribution of raindrop sizes. Radio Sci. 36, 639–642.
Zinevich, A., Alpert, P., Messer, H., 2008. Estimation of rainfall fields using commercial microwave communication networks of variable density. Adv. Water Resour. 31, 1470–1480.